Low-Noise InGaAs/InP Single-Photon Avalanche Diodes for Fiber-Based and Free-Space Applications

Fabio Signorelli, Fabio Telesca, Enrico Conca, Adriano Della Frera, Alessandro Ruggeri, Andrea Giudice, and Alberto Tosi, *Member, IEEE*

***Abstract*—We present the design and the experimental characterization of a new InGaAs/InP single-photon avalanche diode (SPAD), with two different diameters: i) a 10 μm device, suitable for optical fiber-based quantum applications; ii) a 25 μm one, more appropriate for free-space applications. Compared to a previous generation, we improved the design of the double zinc diffusion and optimized the layer structure. We achieved low dark count rate, around 1 kcps and 4 kcps at 225 K and 5 V excess bias for 10 μm and 25 μm devices, respectively, and down to few tens of counts per seconds at 175 K for the 10 μm detector. At 5 V excess bias and 225 K temperature, both devices also show a high photon detection efficiency (33% at 1064 nm, 31% at 1310 nm and 25% at 1550 nm for the 10 μm SPAD). Afterpulsing has been measured with a custom readout integrated circuit, achieving very low probability values. Timing jitter is comparable to previous-generation devices.**

***Index Terms*—InGaAs/InP, single-photon avalanche diode (SPAD), Dark count rate (DCR), detection efficiency, quantum key distribution (QKD), quantum communications.**

I. Introduction

InGaAs/InP Single-Photon Avalanche Diodes (SPADs) are nowadays employed in many applications where single-photon detection in the near-infrared (NIR) range is needed, such as quantum communication [1], quantum optics experiments [2], eye-safe light detection and ranging (LIDAR) [3], deep space optical communication [4], optical time domain reflectometry [5], characterization of semiconductor materials and devices [6], and near-infrared spectroscopy (NIRS) [7]. These devices are among the best candidates for such applications, thanks to their good performance, high reliability, ease of use, compactness and low cost, that are the typical advantages of solid-state detectors. Moreover, SPAD do not need to work at cryogenic temperatures, as opposed to, for example, superconducting nanowire single-photon detectors (SNSPDs). All the above-mentioned applications would benefit from having SPADs with low dark count rate (DCR), in addition to high photon detection efficiency (PDE), low afterpulsing probability and good temporal response.

Manuscript received June 1, 2021; revised August 4, 2021; accepted August 12, 2021. Date of publication August 16, 2021; date of current version September 6, 2021. This work was supported in part by the Autonomous Province of Bozen/Bolzano under the SPIR project (Bando Innovazione 2016). *(Corresponding author: Fabio Signorelli.)*

Fabio Signorelli, Fabio Telesca, Enrico Conca, and Alberto Tosi are with the Dipartimento di Elettronica, Informazione e Bioingegneria Politecnico di Milano, 20133 Milano, Italy (e-mail: fabio.signorelli@polimi.it; fabio.telesca@polimi.it; enrico.conca@polimi.it; alberto.tosi@polimi.it).

Adriano Della Frera, Alessandro Ruggeri, and Andrea Giudice are with the Micro Photon Devices Srl, 39100 Bolzano, Italy (e-mail: adriano.dellafrera@micro-photon-devices.com; alessandro.ruggeri@micro-photon-devices.com; andrea.giudice@micro-photon-devices.com).

Color versions of one or more figures in this article are available at https://doi.org/10.1109/JSTQE.2021.3104962.

Digital Object Identifier 10.1109/JSTQE.2021.3104962

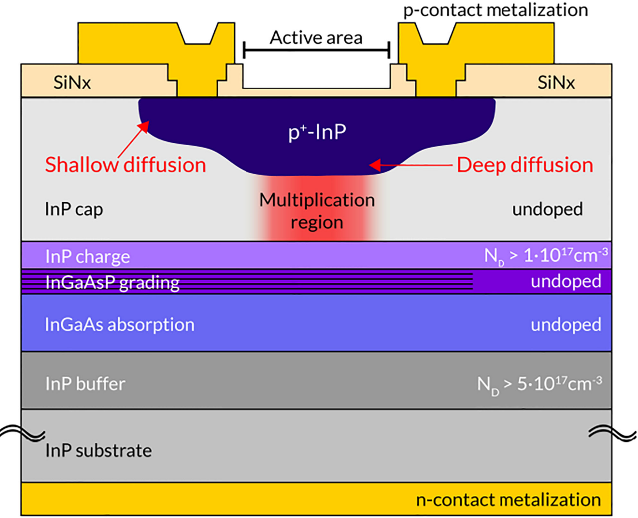

Fig. 1. Schematic representation of the separate absorption, grading, charge and multiplication (SAGCM) heterostructure of the InGaAs/InP SPADs here described. The main regions and layers are labeled in the figure. Photons can enter the device from the aperture on the front-side of the chip and reach the InGaAs absorption region.

In this paper, we present the design of a novel InGaAs/InP SPAD in two different configurations: i) a small device with a 10 μm-diameter active area, intended for optical fiber-based application, where photons can be easily focused within a few-μm spot; ii) a bigger device with 25 μm active area diameter, dedicated to free-space photon-counting applications. The main differences with respect to our previous-generation SPADs are shown, together with experimental results concerning noise, detection efficiency and temporal jitter.

II. Device Structure

The SPADs here described are based on the typical separate absorption, grading, charge and multiplication (SAGCM) heterostructure of InGaAs/InP SPADs, shown in Fig. 1 [8]. A single NIR photon, with wavelength up to about 1.7 μm, is absorbed in the low energy gap non-intentionally doped $In_{0.53}Ga_{0.47}As$ layer ($E_g \sim 0.75$ eV at room temperature) and the photogenerated hole is drifted towards the InP

This work is licensed under a Creative Commons Attribution 4.0 License. For more information, see https://creativecommons.org/licenses/by/4.0/

($E_g \sim 1.35$ eV at room temperature) cap region, where the electric field is high enough to trigger with high probability a self-sustaining avalanche through the impact ionization process [9]. The macroscopic current signal is then easily read by an external circuitry.

In our front-illuminated planar device, a double p^+-zinc diffusion defines the active area of the detector: the deep diffusion ensures a high electric field in the multiplication region, while the shallow diffusion avoids premature edge breakdown at the deep diffusion edge. Moreover, the shallow diffusion lowers the electric field outside the active area enough to avoid the need for a floating guard ring, thus making the devices more compact, which is promising for high-density SPAD arrays with small pixel pitch. In order to guarantee a high electric field in the multiplication region and, at the same time, a low electric field in the absorption region (< 100 kV/cm, high enough to have charge depletion and hole drifting at saturated velocity, but low enough to avoid tunneling), a charge layer is interposed between the multiplication and the absorption layers [10], [11].

Finally, quaternary InGaAsP grading layers are needed between the InGaAs absorption region and the InP-cap layer, so as to reduce the valence band discontinuity that photogenerated holes must overcome to reach the multiplication region.

A. Design of a Low-Noise Detector

Compared to our previous-generation devices, described in [12], the main goal of the new design was to reduce the dark count rate without impairing the photon detection efficiency and, possibly, preserving a good temporal response. Starting from the previous design, we performed technology computer-aided design (TCAD) simulations, both with a commercially available software (Synopsys Sentaurus [13]) and custom MATLAB [14] scripts. We developed a complete electrical simulation model, carefully choosing values and models of the most important electrical parameters, such as the impact ionization model for InP, including their temperature dependence. With such models, we were able to precisely evaluate the effects of any change in the SPAD design on its breakdown voltage, electric field and avalanche triggering probability (i.e., the probability that a free carrier can trigger a self-sustaining avalanche). For an accurate estimation of the PDE, we combined the avalanche triggering probability with optical finite-difference time-domain (FDTD) simulations, which are needed for reliable results, especially for photons absorbed towards the edge of the active area where small lateral and vertical features of the SPAD layers have dimensions comparable with the impinging photon wavelength [15].

Fig. 2 shows an example of TCAD simulation results: we reported the electric field when the device is biased 5 V beyond breakdown and the corresponding avalanche triggering probability in the depleted region. The high electric field is confined below the deep diffusion, but under the shallow diffusion it is still high enough to have a depletion region and help the photogenerated holes to overcome the heterobarrier. The area with high avalanche triggering probability defines the active area of the SPAD, which roughly corresponds to the area below the deep diffusion. A slight increase of such probability (from 70% to 75%) is present at the edge of the deep zinc diffusion. All the simulations were performed at 225 K, which is a typical operating temperature for InGaAs/InP SPADs.

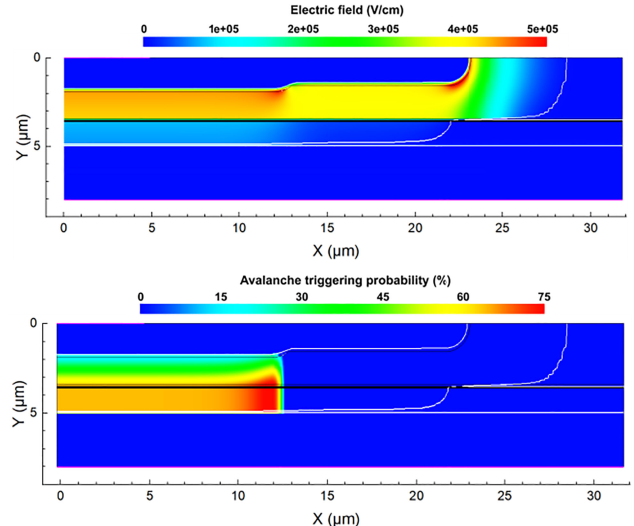

Fig. 2. TCAD simulations of electric field (top) and avalanche triggering probability (bottom) of the 25 μm SPAD, at 225 K and 5 V excess bias. The white lines delimit the depleted region. Only half of the detector is represented.

Concerning the double zinc diffusion, with the support of the new simulation models and of the experimental data of our previous-generation devices, we tailored the depth of both the deep and the shallow diffusions. Fabrication conditions (temperature, phosphine overpressure, and dimethylzinc source flow) were also optimized, starting from the most promising results coming from previous-generation devices, with the aim of reducing even further the defects inside the active region. Our new devices have shallower depths of both the zinc diffusions, while maintaining the InP cap layer thickness unchanged. This resulted in a thicker multiplication region that guarantees a lower electric field above breakdown and, ultimately, reduces field-enhanced carrier generation (e.g., trap-assisted tunneling effects). With respect to our previous-generation SPADs, we increased the charge in the charge layer, achieving a lower electric field in the InGaAs absorption region; this reduces the contribution to DCR of field-enhanced generation from this region, leading to an overall improvement of the device dark count rate [16]. However, the electric field cannot be too small inside the SPAD active volume, otherwise the temporal response of the detector and the charge persistence effect [17], [18] would be degraded. To address such potential issues, we ensured that the hole velocity in the InGaAs layer is still saturated with such low electric field [19], not to worsen the SPAD timing jitter. We also tailored the double zinc diffusion geometry by decreasing the depth difference between the shallow diffusion and the deep one: as a result, the electric field in the InGaAs region below the shallow diffusion is higher and helps the holes (generated in the peripheral regions and that diffuse towards the center of the device) to overcome the heterobarrier towards the InP cap layer before triggering an avalanche. Consequently, their contribution to the charge persistence effect is limited. In

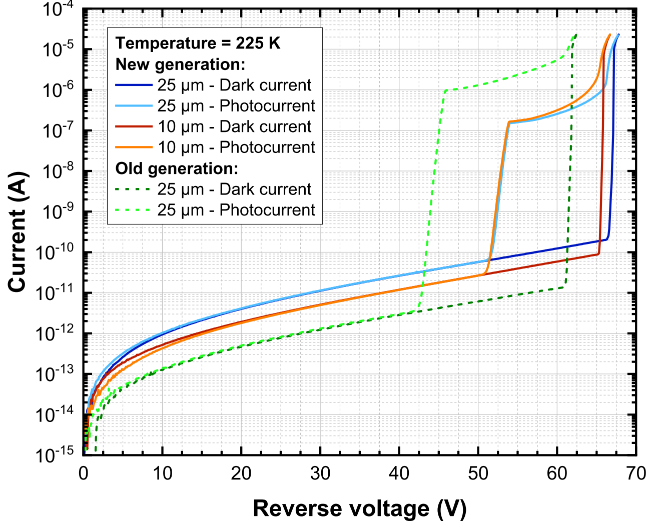

Fig. 3. Current-voltage characteristics of new and old generation devices. Each device was tested both in dark conditions and when illuminated with a continuous-wave 1550 nm laser. Temperature is 225 K. Illumination power is different for measurements on old and new detectors.

addition, a wider-diameter shallow diffusion with respect to the previous-generation SPADs has been employed, so to enlarge the depleted region where holes can easily cross the heterobarrier without triggering an avalanche, again for limiting the charge persistence effect. Moreover, the larger shallow diffusion region helps mitigating non-uniformities of the avalanche triggering probability inside the SPAD active area, which would be more pronounced with the new thicker multiplication region. Finally, the new SPAD structure features five quaternary InGaAsP grading layers (instead of three layers of the previous-generation devices), to further facilitate the heterobarrier crossing probability for photogenerated holes and reduce the temporal jitter on avalanche triggering [10].

III. Experimental Results

The experimental characterization was carried out operating the detector in gated mode with different ON-times, from 2 to tens of nanoseconds. The SPAD is kept 0.5 V below its breakdown voltage during OFF-time, while during ON-time an excess bias voltage (V_{EX}) of few volts (2 V to 7 V) is applied above its breakdown voltage. A simple passive quenching circuit is employed, with a 47 kΩ resistor in series to the SPAD that partially quenches the avalanche current: this resistance value is not sufficient to perform a complete quenching, which is instead granted by lowering the SPAD voltage at the end of the gate ON time.

A. I-V Curve

Fig. 3 shows the current-voltage characteristics of both the 10 μm and the 25 μm active area devices. The breakdown voltage is clearly visible around 65 V in the dark current curves. The steep and sharp increase proves that most of the active region enters in the breakdown regime at such voltage, with negligible edge effects. The breakdown voltage difference between the 10 μm and the 25 μm SPADs could be traced back to the dependence of the zinc diffusion depth on the diffusion mask opening: a smaller diameter mask opening leads to an increased Zn diffusion depth [20]. We also employed a 1550 nm continuous-wave laser to illuminate the SPADs (see "photocurrent" curves) in order to measure the so-called punch-through voltage, i.e., the reverse voltage at which the InGaAs absorption layer starts to be depleted. Such voltage is visible as an increase in the photocurrent around 51 V for both SPADs. When the steep current increase is over (at ~54 V), the InGaAs layer is fully depleted.

Comparing these I-V characteristics with the ones of an old-generation device, it results that the breakdown voltage of new-generation SPADs is few volts higher, as well as the punch-through voltage. This confirms that the electric field both in the multiplication region and in the absorption region has been lowered, thus reducing field-assisted generation of carriers inside the active volume and, ultimately, DCR.

I-V curves of devices with different active-area diameters show that the dark current is proportional to the diameter of the SPAD (the ratio between dark currents of the two devices is ~ 25/10), rather than to its area, thus indicating that the dominant contribution to dark current is peripheral leakage, which does not get multiplied in the active volume of the device and does not generate spurious dark counts. Indeed, new-generation devices show higher dark current with respect to previous-generation ones, but their DCR is lower, as it will be shown in the next section.

B. Dark Count Rate

We measured the primary dark count rate, due to thermal and to field-assisted generation of carriers, of the SPADs at different temperatures and excess bias voltages. In order to rule out afterpulsing phenomena even at low temperatures, all the primary DCR measurements were taken enforcing a 100 μs OFF-time to the SPAD, while ON-time was set to 100 ns, to minimize the impact of the rise and fall times of the square wave (which are about 4.5 ns for these measurements).

As reported in Fig. 4 (top), the 25 μm active-area SPAD shows a DCR of few kcps at 225 K (2300 cps and 4500 cps at 3 V and 5 V excess bias, respectively), a temperature easily achievable with a compact multi-stage thermo-electric cooler inside a small packaging system. By lowering the temperature down to 175 K, the DCR decreases to very low values, e.g., 35 cps and 140 cps at 3 V and 5 V excess bias, respectively.

Even lower dark count rates are achieved by the smaller 10 μm active-area SPAD (Fig. 4, bottom), because of its reduced active volume: at 225 K the DCR is lower than 1 kcps when V_{EX} < 5 V, while at 175 K extremely low DCR values of few tens of counts per second are measured.

For both diameters, when a too high excess bias voltage (V_{EX} ≥ 7 V) is applied, DCR steeply increases due to premature breakdown at the edge of the shallow zinc diffusion.

In our previous work [12], we reported SPADs with DCR of few kcps at 225 K, but mainly referring to selected devices with very low noise. While device screening is possible for specific applications, most of the detectors from a given wafer of the

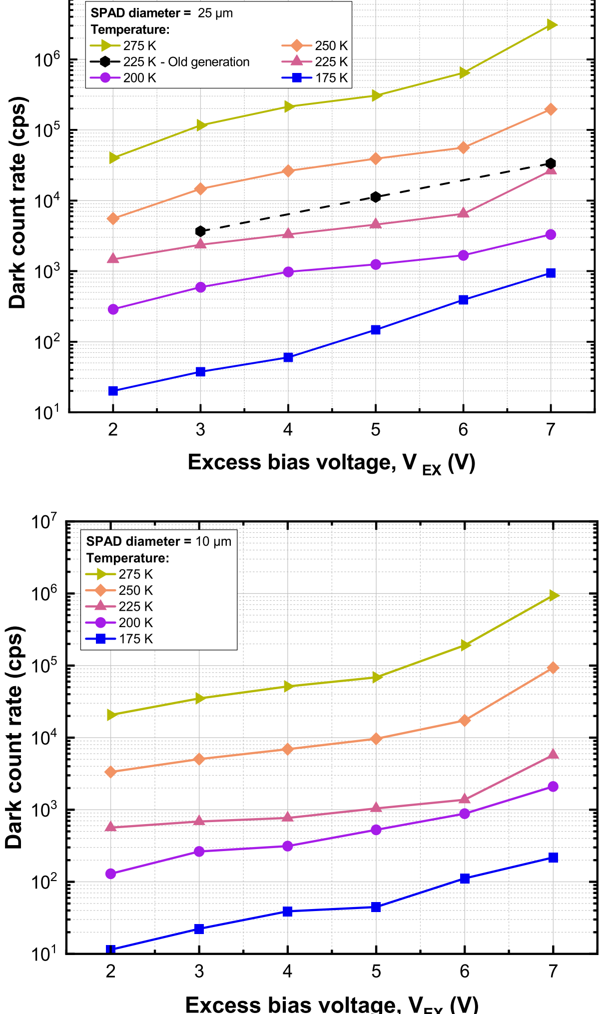

Fig. 4. Primary DCR of the new-generation 25 μm (top) and 10 μm (bottom) active area devices as a function of excess bias voltage at different temperatures. As a reference, we added also the DCR of our 25 μm previous generation device, as measured with the same setup used for the new ones.

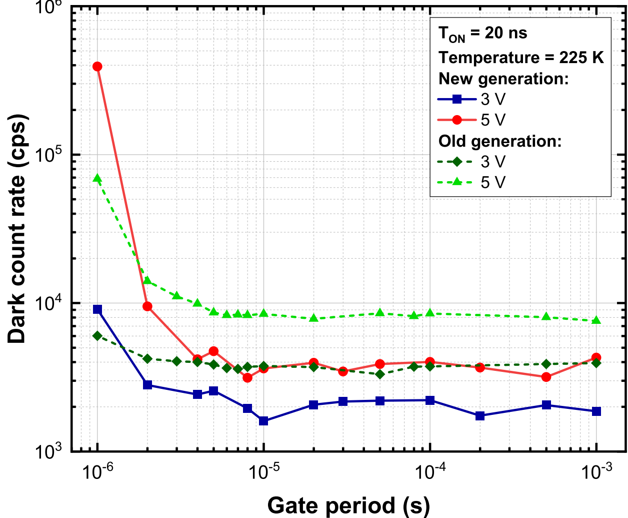

Fig. 5. DCR as a function of the square wave gate period for new and old generation devices, at two excess bias voltages. Gate ON time (T_{ON}) is set to 20 ns. The active area diameter of these detectors is 25 μm.

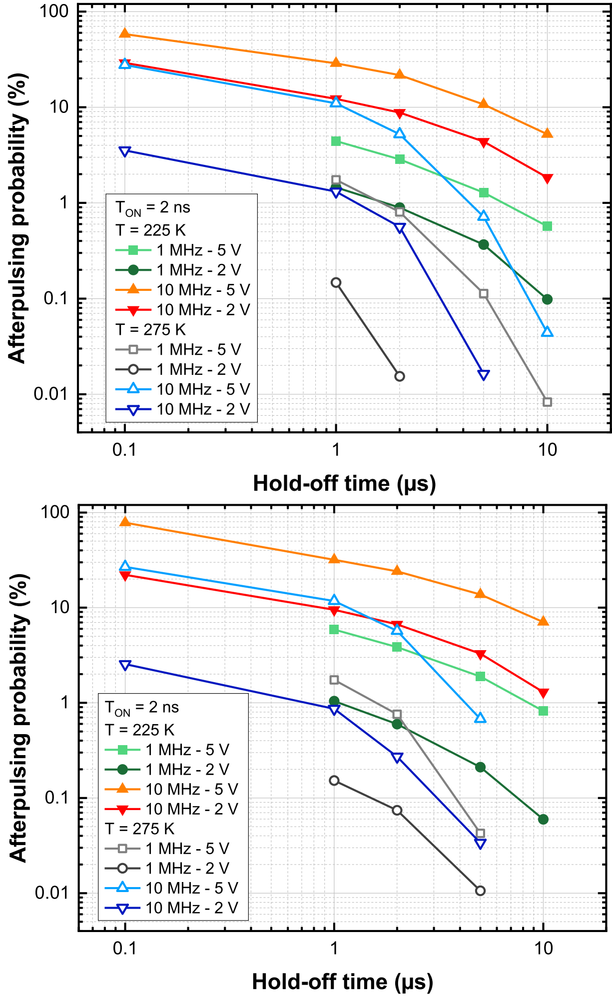

Fig. 6. APP vs. hold-off time for the 10 μm (top) and 25 μm (bottom) SPADs, calculated with TCCC technique, at two different temperatures. Measurements are taken at different V_{EX} and gating frequencies.

previous generation had a DCR of about 10 kcps at 5 V excess bias voltage and at 225 K. In the new generation, most of the InGaAs/InP SPADs in a 3-inch wafer have the DCR shown in Fig. 4, with good uniformity within the wafer. Therefore, there is an improvement of at least 2 times in DCR from old to new generation devices.

C. Afterpulsing

Whenever an avalanche current flows through the SPAD, some carriers may be trapped inside deep-level traps in the InP multiplication region. Such carriers are then released with long time constants (up to few microseconds) and, if one carrier gets released while the SPAD is ON, an avalanche may be triggered, resulting in a subsequent dark count, i.e., an “after-pulse”. Afterpulsing is critical since it affects the linearity of photon-counting measurements and limits the maximum achievable count rate.

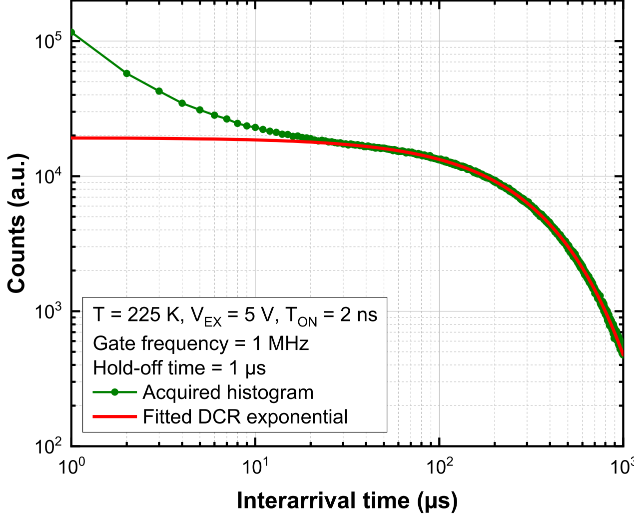

Fig. 7. Example of acquired interarrival time histogram. The red curve represents the exponential, fitted for inter-times between 100 and 1000 μs, of primary DCR. Afterpulsing becomes negligible for interarrival times greater than $\sim$30 μs.

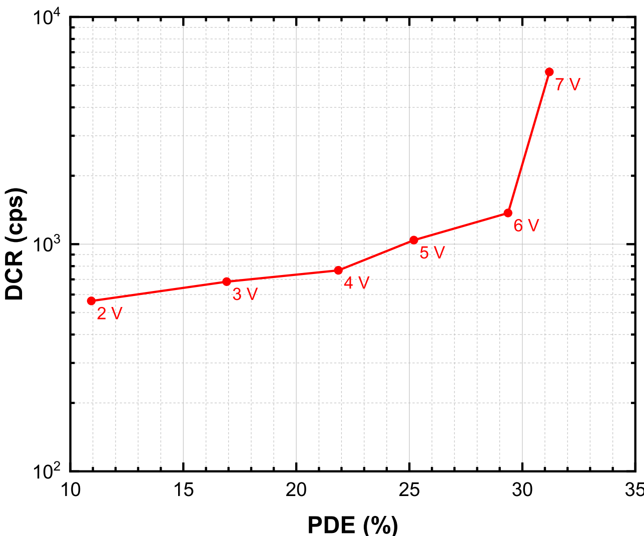

Fig. 8. PDE and DCR of the 10 μm SPAD. The corresponding employed excess bias voltage is reported as a label near each measurement point.

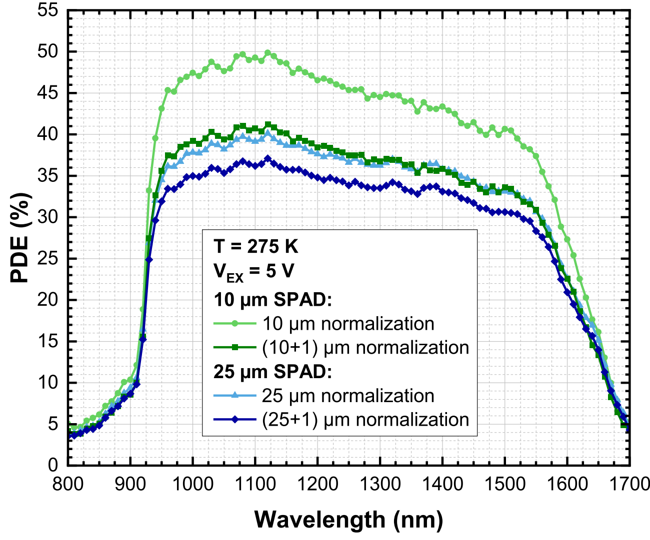

Fig. 9. PDE as a function of wavelength, calculated with two different normalizations for the new-generation SPADs.

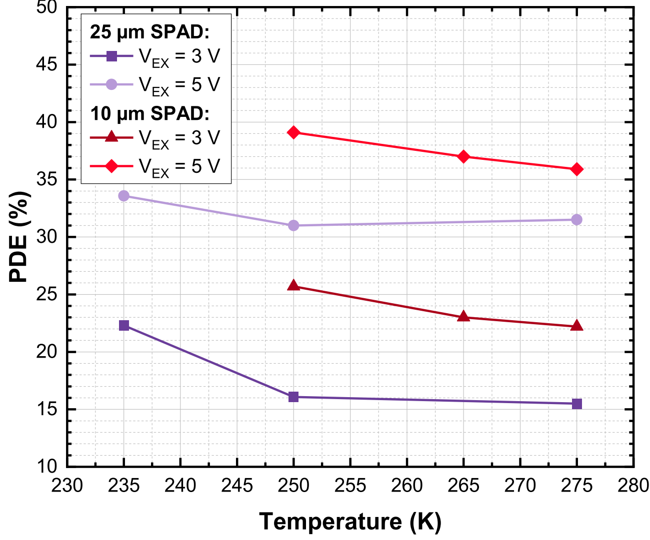

Fig. 10. PDE measured at 1550 nm at different temperature and excess bias voltages for the new-generation devices.

Fig. 5 shows, as an example, the dark count rate of the 25 μm active-area SPAD at 225 K as a function of the gate period, at two different excess bias voltages. When the gate period (almost equal to the OFF time) is lower than about 10 μs, afterpulsing effects exponentially increase, because trapped carriers do not have enough time to be released before the subsequent gate (also called ON time). In the same plot, we also reported a result for a previous-generation SPAD, operated in the same conditions. From a user point-of-view, no substantial difference can be appreciated between the two generations, since approximately the same gate period should be used to avoid severe afterpulsing.

It is worth noting that employing a fast active quenching circuit instead of a simple passive quenching, the afterpulsing is greatly reduced: for example, with the circuit reported in [21], a four-time decrease is obtained. For this reason, we also performed more in-depth measurements on the SPADs by directly wire-bonding them to a newly developed circuit, manufactured in a 0.16 μm BCD (Bipolar-CMOS-DMOS) technology and capable of fast-gating either silicon or InGaAs/InP SPADs at a maximum excess bias of 5 V and a frequency of up to 100 MHz. The integrated circuit employs SPAD – DUMMY differential sensing (detailed afterwards) and a comparator to extract the avalanche signal. This circuit enforces a hold-off time to the SPAD by skipping a programmable number of gate periods after a photon is detected. Quenching of the avalanche current is completed in less than 2 ns, even with long ON-time. The SPAD - DUMMY couple and such frontend chip were hosted onto a carrier PCB with an NTC thermistor for temperature sensing, and placed on top of a 4-stage TEC (thermo-electric cooler) within a custom vacuum chamber.

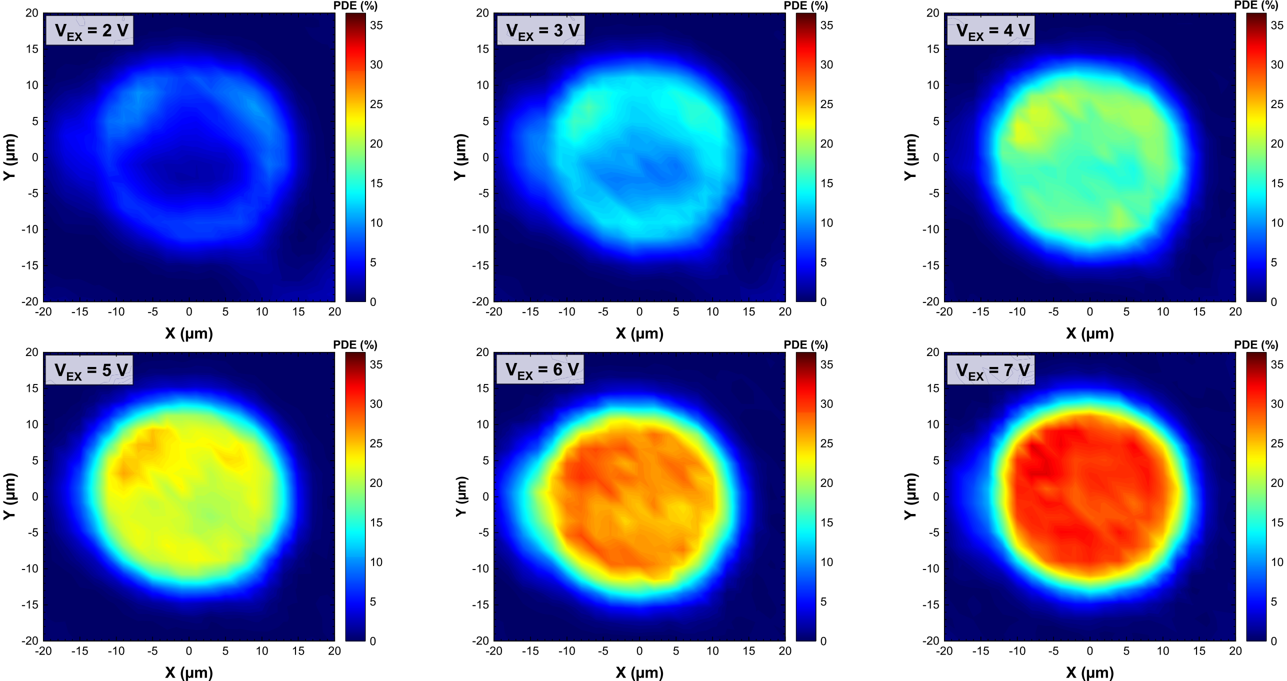

Fig. 11. 2D PDE maps of the 25 μm-active area SPAD at different excess bias voltages, acquired by scanning the active area with a focused 1550 nm continuous wave laser. The light spot is about 6 μm wide. Temperature is 225 K.

Fig. 6 (top) shows the afterpulsing probability (APP), calculated with time-correlated carrier counting (TCCC) technique [22], for the 10 μm diameter SPAD as a function of hold-off time, at different $\mathrm{V_{EX}}$, temperatures and gating frequencies, when the gate width (i.e., ON-time) was set to 2 ns. At 225 K, APP is as low as few percent when the gate frequency is set to 1 MHz, while it is almost 10 times higher with a 10 MHz gating frequency. At higher temperature (275 K), APP is strongly reduced because of faster release times for trapped carriers. Very similar results were also obtained for the 25 μm SPAD, as reported in Fig. 6 (bottom).

An example of interarrival time histogram is shown in Fig. 7: the exponential curve (dashed line) is the fitting of the acquired histogram for interarrival times between 100 μs and 1 ms, thus corresponding to the distribution of just primary DCR. The difference between the acquired histogram and the fitted curve is due to afterpulsing.

D. Photon Detection Efficiency

The photon detection efficiency (PDE) of a SPAD is given by the product of two contributions: i) the absorption efficiency, i.e., the probability that an impinging photon is absorbed in a certain point inside the device; ii) the avalanche triggering probability for carriers generated in that same point. The former is only due to the geometry of the device and to the materials' optical properties; the latter strongly depends on the electric field, which depends on various parameters of the vertical cross-section of the SPAD, e.g., on the InP multiplication region thickness and on doping and shape of the double zinc diffusion.

We measured the photon detection efficiency of the 10 μm device by focusing a 1550 nm continuous wave laser into the active area of the SPAD, with a spot size of about 6 μm. By monitoring the incident light power with a calibrated photodiode, we calculated the photon flux on the detector (attenuated to the single-photon level) and eventually the PDE in each point of the device. Fig. 8 shows the DCR as a function of the PDE, rather than the applied excess bias voltage. This representation can be useful for a fair comparison between different devices from different production runs or from different manufacturers, which may be designed to work at very different excess bias voltages. The 6 μm spot size well matches the spot size in a single-mode fiber pigtailing system, where photons are focused in a spot of about 5 μm on the detector. PDE reaches 24% with DCR lower than 1000 cps, and it is still more than 10% with DCR $<$ 600 cps.

We also measured the spectral PDE by uniformly illuminating the whole chip area, employing a broad-band light source, a monochromator, and an integrating sphere. The measurement was performed from 800 nm to 1700 nm, with 10 nm steps. A critical point to estimate the PDE is the area used for calculating the impinging photon flux. A first approach is to consider as active area the deep diffusion aperture, e.g., a 25 μm circle for the larger SPAD. However, a more correct definition of active-area takes into account the surrounding area where the avalanche triggering probability is not zero (see Fig. 2, bottom), which we estimated from simulations to be about 1 μm wider in diameter with respect to the deep diffusion aperture. In Fig. 9, we reported the PDE calculated with both the normalizations.

When all the die area is flood illuminated, the charge persistence effect can affect the measurement: photons absorbed

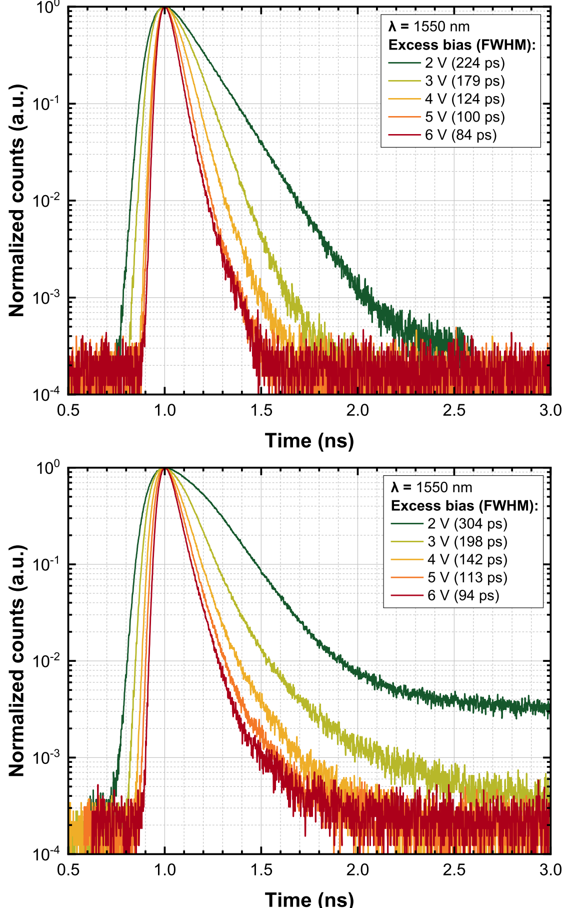

Fig. 12. Temporal response of the 10 μm-active area SPAD, measured with a 6 μm laser spot focused inside the active area (top) ad with flood illumination over the whole die area (bottom). Laser wavelength is 1550 nm. Temperature is 240 K.

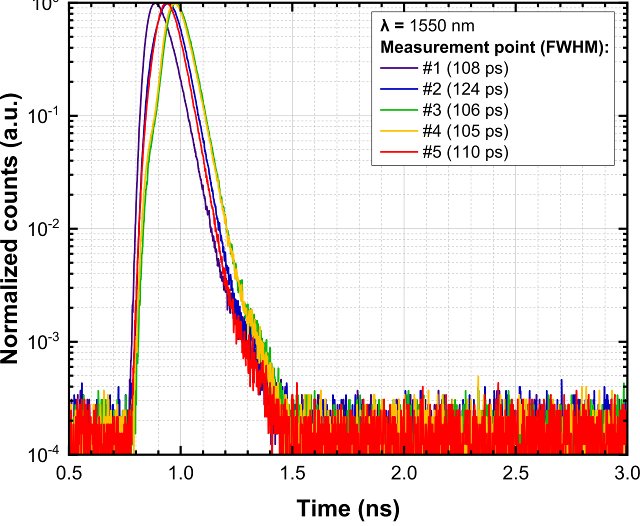

Fig. 13. Temporal response of the 25 μm-active area SPAD, measured with a 6 μm laser spot focused inside the active area in five different locations, sampling regions with different PDE according to the maps shown in Fig. 11, corresponding to regions with different local electric field. Laser wavelength is 1550 nm. Temperature is 240 K and excess bias is 5 V.

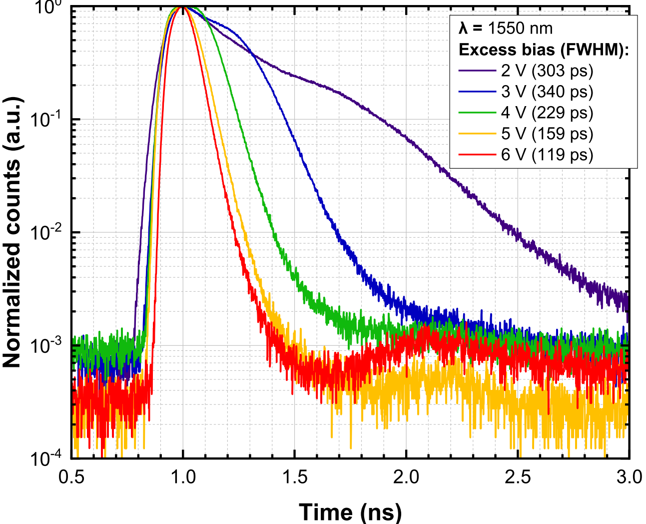

Fig. 14. Temporal response of the 25 μm-active area SPAD, measured with flood illumination over the whole die area, at different excess bias voltages. Laser wavelength is 1550 nm. Temperature is 240 K.

outside the active area can diffuse, during OFF-time, towards the high field region and trigger an avalanche [17][18]. This causes an abnormal increase in the PDE, since the normalization area for PDE estimation does not include the entire collection area, which should involve the SPAD surroundings. Therefore, in order to verify the impact of charge persistence in this measurement and, possibly, to minimize its contribution, we performed the PDE measurements at different temperatures. Increasing the temperature, the hole lifetime in the InGaAs layer exponentially decreases and, at the same time, the electric field at the heterointerface gets higher (since the breakdown voltage increases as well). According to [17], about 10 times reduction every 25 K is expected. This effect is more evident in smaller devices, since the peripheral region where charge persistence occurs is bigger in proportion to the SPAD active area. Fig. 10 shows the PDE measured at 1550 nm and at different temperatures: as expected, the higher the temperature, the lower the estimated PDE. Above a certain temperature, the measured PDE value stabilizes. For these reasons, the spectral PDE curves here reported are measured at 275 K, so to guarantee a correct estimation of PDE with negligible distortion from the charge persistence.

Up to about 900 nm, the incident photons are absorbed in the InP cap layer, above the p-n junction, where the photogenerated electrons diffuse towards the high-field multiplication region. At longer wavelengths, beyond the InP cutoff ($\sim$920 nm), all the photons are absorbed into the InGaAs layer and the PDE reaches values higher than 35% between 1000 and 1200 nm. Near the cutoff wavelength of InGaAs ($\sim$1600 nm), the PDE rapidly decreases down to 5% at 1700 nm. All the reported measurements were performed at 5 V excess bias, with 10 kHz repetition rate and 100 ns gate width.

Comparing the 25 μm and the 10 μm SPADs, the latter has a higher PDE throughout all the wavelengths (33% at 1064 nm, 31% at 1310 nm and 25% at 1550 nm, at 5 V excess bias),

TABLE I
SUMMARY OF PERFORMANCE AND COMPARISON WITH STATE-OF-THE-ART InGaAs/InP SPADs

Ref.	Year	Active area diameter (µm)	Temperature (K)	DCR (cps) @ PDE (%)	APP (%) @ HO time (ns)[a]	Timing jitter (ps) @ PDE (%)
This work (10 µm)	2021	10	225	560 - 1370 @ 11 - 30	1.4 - 4.4 @ 1000	225 - 84 @ 11 - 30
This work (25 µm)	2021	25	225	1460 - 6470 @ 11 - 30	1 - 5.9 @ 1000	340 - 119 @ 11 - 30
Baek *et al.* [23]	2021	16	233	1.4 k - 4 k[b] @ 21 - 31	2 - 7[c]	N.A.
			293	20 k - 100 k[b] @ 21 - 31	1 - 2.5[c]	
Fang *et al.*[24]	2020	25	233	260 - 2.5 k @ 7 - 37	4.8 - 12.5 @ < 0.8[c]	N.A.
			253	900 - 21.6 k @ 7.5 - 46	1.4 - 12.6 @ < 0.8[c]	
Park *et al.* [25]	2019	N.A.	253	14.4 k - 16.8 k[d] @ 10.2 - 25.3	0.69 - 21.62 @ 160	N.A.
Tamura *et al.* [26]	2018	9	233	22.2 k - 111.1 k[e] @ 10 - 48[f]	61.5 - 90	450 - 400 @ 10 - 50
			253	111 k - 277 k[e] @ 8 - 17[f]	47 - 85	580 - 450 @ 8 - 17
Baba *et al.* [27]	2018	12	242	234 k @ 10	86.4 - 25[g] @ 25 - 800	260[h]
Jiang *et al.* [28]	2018	N.A.	253	1.4 k - 3.2 k @ 10 - 25	N.A.	N.A.

[a]HO = hold-off, only reported when available. [b]Computed from dark count probability per gate, with gate frequency = 10 MHz, gate width = 2 ns. [c]Changes with gate signal amplitude. [d]Computed from dark count probability per gate, with gate frequency = 1 GHz, gate width = 400 ps. [e]DCR of the single pixel computed as 1/9th of the DCR of a 3×3 array. [f]Afterpulse probability not subtracted. [g]Measurement conditions: T = 251 K, V_{EX} = 1.9 V. [h]Measurement conditions: T = 255 K, V_{EX} = 1.6 V.

because field enhancement effects at the edge of the active area dominate with respect to the uniform central region, where electric field is slightly lower. The smaller the SPAD diameter, the more this effect is evident.

Finally, Fig. 11 shows 2D PDE maps acquired at different excess bias voltages on the 25 μm active-area SPAD. The 6 μm-wide laser spot is moved with 1 μm steps in both x and y directions, and the PDE is locally measured. The active area uniformity at different working conditions can thus be assessed: at low excess bias voltages (below 3 V), the PDE is higher on the edge of the active area, where the edge curvature of the deep zinc diffusion enhances the electric field and, so, also the avalanche triggering probability. At higher excess bias voltages, the PDE in the active area is more uniform, because of saturation of the avalanche triggering probability.

E. Timing Jitter

Timing jitter of a SPAD indicates the statistical spread of the delay between the arrival of a photon and the output electrical pulse. We measured the timing performance of our detectors by illuminating them with a pulsed laser at 1550 nm wavelength. The FWHM of the laser pulse is nominally 18 ps and timing data were acquired with a standard TCSPC setup (intrinsic resolution of 8 ps FWHM). In order to read the SPAD avalanche signal with a very low threshold (to limit the timing jitter on the avalanche build-up), we employed a SPAD – DUMMY approach and a fast differential comparator (with a timing jitter of few picoseconds) [21]. The dummy device is integrated in the same chip of the SPAD and mimics all the stray SPAD capacitances and inductances. Its structure is very similar to the one of the SPAD, but there is no deep zinc diffusion in order to have a higher breakdown voltage, while still guaranteeing a correct capacitive matching. Fig. 12 (top) shows the temporal response of the 10 μm device, when the laser is focused only inside its active area (as when a fiber is pigtailed to the SPAD). At 2 V excess bias, the FWHM is 225 ps, and it reduces to 84 ps when $V_{EX} = 6$ V. The full width at 1/100 of the maximum ranges between 850 ps at $V_{EX} = 2$ V and 300 ps at 6 V excess bias, while the width at 1/1000 of the peak is between 1.2 ns and 450 ps, respectively.

The temporal response of the 10 μm device slightly worsens if the laser is no more focused just on the active area, but the whole chip is illuminated. FWHM in such conditions are about 10% worse than the previous case and a longer tail is present (see Fig. 12, bottom), due to the charge persistence effect (carriers photogenerated around the active area diffuse towards the central high field region and might trigger avalanches with some delay).

Concerning the 25 μm SPAD, when the pulsed laser is focused within a 6 μm spot inside its active area, the temporal response is quite similar to the one of the 10 μm SPAD, but with slightly higher jitter (106 ps at 5 V excess bias, compared to 100 ps of the 10 μm device). However, moving the spot around the active area, the temporal response shape changes and the main peak position moves: Fig. 13 shows the temporal response of the device when the laser spot is focused in 5 different locations inside the active area, each one with a slightly different local PDE (see the map corresponding to $V_{EX} = 5$ V in Fig. 11 as an example of local PDE variations). Such non-uniform temporal response can be ascribed to a non-uniformity of the local electric field, which can be traced back to small changes in the zinc diffusion depth. However, despite these non-uniformities, the timing jitter of the 25 μm SPAD is as low as 159 ps (FWHM) at 5 V excess bias. The impact of such non-uniform electric field is stronger at lower excess bias voltages (see Fig. 14).

IV. Conclusion

In this paper, we presented the design of a low noise InGaAs/InP SPAD with 10 μm and 25 μm active area diameter. Starting from TCAD simulations, we tailored the electric field inside the SPAD device, in order to reduce it both in the multiplication region and in the absorption region. To this aim, we optimized the zinc diffusion conditions, as wells as the charge layer doping. Moreover, in order to limit charge persistence effects, we tuned the depth and the diameter of both deep and shallow diffusions. Increasing the number of quaternary grading layers from three to five also helped in reducing charge persistence and hole pile-up at the heterointerface.

25% PDE is obtained at 225 K, with a DCR around 1000 cps and 4 kcps for 10 μm and 25 μm devices, respectively, which correspond to a noise equivalent power (NEP) of $2.3 \cdot 10^{-17}$ W/Hz^{½} and $4.6 \cdot 10^{-17}$ W/Hz^{½}. At the lower temperature of 175 K, extremely low DCR of tens of counts per second are reported. The timing response shows a narrow peak for the 10 μm SPAD (FWHM is 100 ps at 5 V excess bias), while it is wider for the 25 μm detector due to small non-uniformity of the zinc diffusion, an issue that will be tackled in the next fabrication run. Afterpulsing probability of few percent was achieved at 225 K for both devices, enabling a maximum photon count rate of about 1 MHz.

Table I reports a performance summary of the SPADs here presented, together with other state-of-the-art InGaAs/InP SPADs reported in recent literature. Comparing different devices at similar PDE, our detectors show low DCR and very low afterpulsing, despite the lower operating temperature, thanks to the dedicated integrated circuit, and best-in-class timing jitter.

In conclusion, the achieved results make the InGaAs/InP SPAD here presented an excellent candidate for optical fiber-based and free-space quantum applications in the near-infrared range.

References

[1] N. Gisin and R. Thew, "Quantum communication," *Nat. Photon.*, vol. 1, no. 3, pp. 165–171, Mar. 2007.

[2] M. Davanço *et al.*, "Telecommunications-band heralded single photons from a silicon nanophotonic chip," *Appl. Phys. Lett.*, vol. 100, no. 26, Jun. 2012, Art. no. 261104.

[3] Y. U. Chao *et al.*, "Fully integrated free-running InGaAs/InP single-photon detector for accurate lidar applications," *Opt. Exp.*, vol. 25, no. 13, pp. 14611–14620, Jun. 2017.

[4] R. J. Cesarone, D. S. Abraham, S. Shambayati, and J. Rush, "Deep-space optical communications," in *Proc. Int. Conf. Space Opt. Syst. Appl.*, pp. 410–423, May 2011.

[5] P. Eraerds, J. Zhang, H. Zbinden, N. Gisin, and M. Legré, "Photon counting OTDR: Advantages and limitations," *J. Light. Technol.*, vol. 28, no. 6, pp. 952–964, Mar. 2010.

[6] F. Stellari, P. Song, and A. J. Weger, "Single-photon detectors for ultra-low-voltage time-resolved emission measurements of VLSI circuits," in *Proc. SPIE Adv. Photon Counting Techn. V*, May 2011, Art. no. 803317.

[7] S. A. Carp *et al.*, "Diffuse correlation spectroscopy measurements of blood flow using 1064 nm light," *J. Biomed. Opt.*, vol. 25, no. 09, pp. 97003–97004, Sep. 2020.

[8] J. C. Campbell, A. G. Dentai, W. S. Holden, and B. L. Kasper, "High-performance avalanche photodiode with separate absorption 'grading' and multiplication regions," *Electron. Lett.*, vol. 19, no. 20, pp. 818–820, Sep. 1983.

[9] Y. Okuto and C. R. Crowell, "Energy-conservation considerations in the characterization of impact ionization in semiconductors," *Phys. Rev. B*, vol. 6, no. 8, pp. 3076–3081, Oct. 1972.

[10] F. Acerbi, M. Anti, A. Tosi, and F. Zappa, "Design criteria for InGaAs/InP single-photon avalanche diode," *IEEE Photon. J.*, vol. 5, no. 2, pp. 6800209–6800209, Apr. 2013.

[11] J. Ma *et al.*, "Design considerations of high-performance InGaAs/InP single-photon avalanche diodes for quantum key distribution," *Appl. Opt.*, vol. 55, no. 27, pp. 7497, Sep. 2016.

[12] A. Tosi, N. Calandri, M. Sanzaro, and F. Acerbi, "Low-noise, low-jitter, high detection efficiency InGaAs/InP single-photon avalanche diode," *IEEE J. Sel. Topics Quantum Electron.*, vol. 20, no. 6, pp. 192–197, Nov. 2014.

[13] TCAD Sentaurus R-2020.09. Synopsys, 2020.

[14] MATLAB R2020b. MathWorks, 2020.

[15] F. Signorelli, F. Telesca, and A. Tosi, "Photon detection efficiency simulation of InGaAs/InP SPAD," in *Proc. Int. Conf. Numer. Simul. Optoelectronic Devices*, Sep. 2020, pp. 21–22.

[16] A. B. Mehdi, X. Lou, M. Dong, L. Zhu, and C. Li, "InGaAs/InP single-photon avalanche diodes performance variation with charge layer width and doping," in *Proc. IEEE 13th Int. Conf. Electron. Meas. Instrum.*, Jul. 2017, pp. 286–290.

[17] N. Calandri, M. Sanzaro, A. Tosi, and F. Zappa, "Charge persistence in InGaAs/InP single-photon avalanche diodes," *IEEE J. Quantum Electron.*, vol. 52, no. 3, pp. 1–7, Mar. 2016.

[18] Y. S. Lee, K. Y. Chen, S. Y. Chien, and S. C. Chang, "Characteristics of charge persistence in InGaAs/InP single-photon avalanche diode," *IEEE Photon. Technol. Lett.*, vol. 30, no. 22, pp. 1980–1982, Nov. 2018.

[19] P. Hill *et al.*, "Measurement of hole velocity in n-type InGaAs," *Appl. Phys. Lett.*, vol. 50, no. 18, pp. 1260–1262, Jun. 1987.

[20] R. Ben-Michael, M. A. Itzler, and X. Jiang, "Method for dopant diffusion," US Patent 2008/0220598 A1, Sep. Nov., 2008.

[21] F. Acerbi, A. Della Frera, A. Tosi, and F. Zappa, "Fast active quenching circuit for reducing avalanche charge and afterpulsing in InGaAs/InP single-photon avalanche diode," *IEEE J. Quantum Electron.*, vol. 49, no. 7, pp. 563–569, Jul. 2013.

[22] S. Cova, A. Lacaita, and G. Ripamonti, "Trapping phenomena in avalanche photodiodes on nanosecond scale," *IEEE Electron. Device Lett.*, vol. 12, no. 12, pp. 685–687, Dec. 1991.

[23] S.-H. Baek *et al.*, "Room temperature quantum key distribution characteristics of low-noise InGaAs/InP single-photon avalanche diode," *J. Korean Phys. Soc.*, vol. 78, no. 7, pp. 634–641, Mar. 2021.

[24] Y. Q. Fang *et al.*, "InGaAs/InP single-photon detectors with 60% detection efficiency at 1550 nm," *Rev. Sci. Instrum.*, vol. 91, no. 8, pp. 083102, Aug. 2020 .

[25] C.-Y. Park, S.-B. Cho, C. Park, S. Baek, and S.-K. Han, "Dual anode single-photon avalanche diode for high-speed and low-noise Geiger-mode operation," *Opt. Exp.*, vol. 27, no. 13, pp. 18201–18209, Jun. 2019.

[26] Y. Tamura et al.*et al.*, "Development of ingaas MPPC for NIR photon counting applications," *Proc. SPIE, Optical Components Materials XV*, p. 105280Z, Feb. 2018.

[27] T. Baba *et al.*, "Development of an InGaAs SPAD 2D array for flash LIDAR," in *Proc. 15th SPIE Quantum Sens. Nano Electron. Photon.*, Jan. 2018, Art. no. 105400L.

[28] X. Jiang *et al.*, "InGaAsP/InP Geiger-mode APD-based LiDAR," in *Proc. SPIE Opt. Sens. Imag. Photon Counting: From X-Rays THz*, Sep. 2018, Art. no. 107290C.

Fabio Signorelli was born in Bergamo, Italy, in 1994. He received the bachelor's and M.Sc. degrees in 2016 and 2018, respectively, in electronics engineering from Politecnico di Milano, Milan, Italy, where he has been working toward the Ph.D. degree in information technology since November 2018. His research interests include the design, development, and characterization of visible and near-infrared single-photon avalanche diodes (SPADs) and SPAD arrays in Silicon, Germanium, and InGaAs/InP semiconductors.

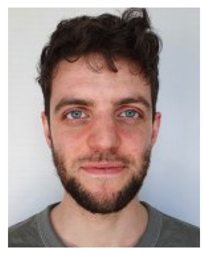

Fabio Telesca was born in Melfi, Italy, in 1994. He received the bachelor's degree in 2017 (cum laude) in biomedical engineering and the master's degree in 2020 (cum laude) in electronics engineering from Politecnico di Milano, Milan, Italy, where he has been working toward the Ph.D. degree in information technology. His current research focuses on the characterization and design of InGaAs/InP single-photon avalanche diodes for near-infrared applications.

Enrico Conca was born in Cremona, Italy, in 1992. He received the master's degree (cum laude) in electronics engineering and the Ph.D. degree in information technology from Politecnico di Milano, Milan, Italy, in 2016 and 2019, respectively. He is currently a Postdoc Researcher with the Department of Electronics, Information and Bioengineering, Politecnico di Milano. His research focuses on the design and development of time-gated single photon counting circuits in CMOS and BCD technologies.

Adriano Della Frera was born in Milan, Italy, in 1983. He received the master's degree in electronics engineering from Politecnico di Milano, Milan, Italy, in 2009. He was a Research Assistant with the Dipartimento di Elettronica e Informazione, Politecnico di Milano and as a Freelancer. In 2018, he moved to Micro Photon Devices (Bozen), as a Product R&D Manager. His current research interests include InGaAs/InP and silicon single-photon detectors and the development of the related electronics for product development.

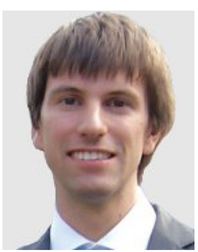

Alessandro Ruggeri was born in Alzano Lombardo, Italy, in 1987. He received the master's degree in electronics engineering and the Ph.D. degree in information technology from Politecnico di Milano, Milan, Italy, in 2012 and 2015, respectively. As student, he worked on optical testing of VLSI circuits with IBM T. J. Watson Research Center, Yorktown Heights, NY, USA. After a few years as a R&D Designer, he is currently the Chief Technology officer with Micro Photon Devices, Bolzano, Italy. His main research interest regards the development of electronics for visible and near-infrared single-photon avalanche diodes for biomedical, quantum sensing, and communication applications.

Andrea Giudice received the Ph.D. degree in electronic and communication engineering from Politecnico di Milano, Milan, Italy, in 2003. He is currently the Managing Director of Micro Photon Devices (MPD), expert in the design, validation, and characterisation of electronic devices and circuits. In 1997, he was a Summer Student with National Microelectronics Research Centre (NMRC now Tyndall), Cork, Ireland, where he designed and tested avalanche photodiodes for single-photon detection. Deep know-how in single-photon detectors and applications gained during his Ph.D. with Prof. Cova's Group and during his previous career in MPD, as a Senior R&D Engineer.

Alberto Tosi (Member, IEEE) was born in Borgomanero, Italy, in 1975. He received the master's degree in electronics engineering and the Ph.D. degree in information technology engineering from Politecnico di Milano, Milan, Italy, in 2001 and 2005, respectively. From 2006 to 2014, he was an Assistant Professor. Since 2014, he has been an Associate Professor of electronics with Politecnico di Milano. In 2004, he was a Student with IBM T. J. Watson Research Center, Yorktown Heights, NY, USA, working on optical testing of CMOS circuits. He currently works on silicon and InGaAs/InP single-photon avalanche diodes (SPADs). His research interests include arrays of silicon SPADs for 2-D and 3-D applications and time-correlated single-photon counting electronics.